Ti_1/graphene single-atom material for highly efficient and stable perovskite solar cells

Chunyang Zhang[1,2], Suxia Liang[3], Wei Liu[1], Felix T. Eickemeyer[2], Xiangbin Cai[4], Ke Zhou[5], Jiming Bian[6], Hongwei Zhu[2], Chao Zhu[7*], Ning Wang[4], Zaiwei Wang[8], Jiangwei Zhang[3], Yudi Wang[1], Jinwen Hu[1], Hongru Ma[1], Cuncun Xin[1], Shaik Mohammed Zakeeruddin[2], Michael Grätzel[2*] and Yantao Shi[1,*]

[1]State Key Laboratory of Fine Chemicals, Department of Chemistry, School of Chemical Engineering, Dalian University of Technology, Dalian, 116024, China. Email: shiyantao@dlut.edu.cn

[2]Laboratory of Photonics and Interfaces (LPI), Department of Chemistry and Chemical Engineering, École Polytechnique Fédérale de Lausanne (EPFL), CH-1015 Lausanne, Switzerland. Email: michael.graetzel@epfl.ch

[3]State Key Laboratory of Catalysis, Dalian Institute of Chemical Physics, Chinese Academy of Sciences, Dalian, 116023, China.

[4]Department of Physics, Hong Kong University of Science and Technology, Kowloon, Hong Kong, China.

[5]Department of Chemistry & College of Chemistry and Chemical Engineering, Xiamen University, Xiamen 361005, China.

[6]Key Laboratory of Materials Modification by Laser, Ion and Electron Beams (Ministry of Education), School of Physics, Dalian University of Technology, Dalian 116024, China.

[7]SEU-FEI Nano-Pico Center, Key Laboratory of MEMS of Ministry of Education, Collaborative Innovation Center for Micro/Nano Fabrication, Device and System, Southeast University, Nanjing 210096, P. R. China. Email: phczhu@seu.edu.cn

[8]Laboratory of Photomolecular Science (LSPM), École Polytechnique Fédérale de Lausanne, Station 6, CH-1015 Lausanne, Switzerland.

C. Y. Zhang, S. X. Liang and W. Liu contributed equally.

Abstract

Carbon-based perovskite solar cells (C-PSCs) are widely accepted as stable, cost-effective photovoltaics. However, C-PSCs have been suffering from relatively low power conversion efficiencies (PCEs) due to severe electrode-related energy loss. Herein, we report the application of a single-atom material (SAM) as the back electrode in C-PSCs. Our Ti_1/rGO consists of single titanium (Ti) adatoms anchored on reduced graphene oxide (rGO) in a well-defined Ti_1O_4-OH configuration capable of ~~well~~ tuning the electronic properties of rGO. The downshift of the Fermi level notably minimizes the series resistance of the carbon-based electrode. By combining with an advanced modular cell architecture, a steady-state PCE of up

to 20.6% for C-PSCs is finally achieved. Furthermore, ~~the device without encapsulation tracked at the maximum power point under one-sun illumination retains 90% of its initial value after 1000 h.~~the devices without encapsulation retain 98% and 95% of their initial values for 1300 h under 1-sun illumination at 25 ^{o}C and 60 ^{o}C, respectively.

Introduction

Perovskite solar cells (PSCs) as the emerging 3rd generation photovoltaics have experienced rapid development over the past ten years and achieved a certificated high power conversion efficiencies (PCEs) of 25.5% to date[1]. However, the stability issue remains the major obstacle slowing down the large-scale application of PSCs[2-8]. Studies in recent years reveal that the most widely used Ag or Au back electrodes in traditional PSCs is one of the main sources leading to the deterioration of cell performance as they corrode easily, where the metallic bonds (Ag-Ag or Au-Au) are apt to be broken by the iodide from the perovskite layer underneath[6,9,10]. Replacing metal back electrodes with carbon-based ones has been validated to be a good strategy[11-13]. The hydrophobic nature as well as the stable covalent bond structure endows carbon-based back electrodes with excellent moisture resistance and chemical stability, avoiding the corrosion as mentioned above[13]. In general, the stability of C-PSCs is much better than that of traditional PSCs[7,12-14]. Despite being widely accepted as the stable, cost-effective and large-scale processable photovoltaics, C-PSCs have been suffering from severe energy loss caused by the carbon electrode itself and the carbon/perovskite or carbon/spiro-OMeTAD interface[14-16]. As a consequence, the PCEs of C-PSCs are generally much lower than those of traditional PSCs[12-14], mostly in a wide range between 10% ~ 18 % as statistically summarized from relevant reports (Supplementary Fig. 1 and Supplementary Table 1)[17,18]. The key to increase efficiencies to the same level as thermal evaporation metal-based PSC is to minimize the energy loss originating from the retarded rate of charge transport and transfer, which comes

from the large sheet resistance of carbon electrode, the poor interfacial contact and mismatched band alignment between carbon electrode and adjacent functional layer[15,19,20].

As a unique two-dimensional (2D) carbon material, graphene has been regarded as a good back contact candidate for C-PSCs owing to its excellent electrical properties (such as high conductivity and tunable energy level)[14,15,21]. Over the past few years, back electrodes based on graphene or its composites have been intensively exploited for C-PSCs[15,21-23]. However, the PCEs of corresponding devices are only around 10% ~12% in most previous reports (Supplementary Fig. 2)[15,16,21-23]. Tuning the electrical properties of graphene, such as through heteroatoms doping (like N, O, S, P), has been applied to boost the PCE of C-PSCs[16,24]. An example reported by Zhu and coworkers in 2018 indicated that, owing to the increased charge-extraction efficiency and transport capability, the N-doped graphene framework as the back electrodes enabled the PCE of C-PSCs to be enhanced from 9.0% to 10.3% with respect to the un-doped sample[16]. In recent years, the increasing theoretical prediction and experimental demonstration show that the electrical properties of graphene, e.g., the work function, can be well regulated by the decoration of metal nanoparticles or metal salts[25,26]. However, the inhomogeneity of the distribution of metal species and their ambiguous bonding configurations with the graphene pose a serious obstacle to clearly identifying the precise structure at atomic level and to further establishing the structural correlation with the electrical properties.

Featuring atomically dispersed metal atoms and well-defined coordination structures on solid substrates, single-atom materials (SAMs) have emerged as an exciting class of materials with many appealing advantages for heterogeneous catalysis (in this field, they are usually termed as single-atom catalysts, SACs)[27-31]. However, so far SAMs have scarcely been applied or investigated in the photoelectric field[30,31]. Herein, we report the application of SAM as the back contact in all-solid-state solar cells. Our SAM of Ti_1/rGO consists of single titanium (Ti) adatoms anchored by surface oxygen atoms on the rGO in a well-defined configuration. DFT

calculations indicate the evident charge transfer between rGO and Ti adatoms, which leads to notable variations in the electronic structure with regard to the bare rGO, in good consistence with the subsequent experimental validation. As a result, the downshift of Fermi level notably minimizes the series resistance of the carbon-based transport layer minimizing the energy loss. By combining with an advanced modular cell architecture, a high steady-state PCE up to 20.6% is finally achieved by our Ti_1/rGO-based C-PSCs, evidently higher than that (17.5%) of the control device based on the bare rGO. Furthermore, the Ti_1/rGO-based C-PSC without encapsulation cells retain 98% and 95% of their initial PCE values during light soaking with full solar intensity under maximum power point tracking for 1300 h under nitrogen at 25 ^{o}C and 60 ^{o}C, respectively.

Results and Discussions

Structural characterizations of Ti_1/rGO

The X-ray photoelectron spectroscopy (XPS) analysis exhibits that unlike the ideal graphene, the residual oxygen on rGO is still abundant (~10 at. %) even after a thermal reduction treatment at 550 ^{o}C (Supplementary Fig. 3a). The high-resolution XPS C 1s spectrum (Supplementary Fig. 3b) reveals that the residual oxygen exists in the form of mixed oxygen-containing species, such as hydroxyl (-OH), epoxide (C-O-C), and carboxyl (C-OO). These oxo species provide potential anchoring sites for Ti adatoms according to the strong interaction between Ti and O atoms. Accordingly, the Ti_1/rGO SAM sample was prepared via a simple chemisorption route (Fig. 1a).

Fig. 1b and 1c show the SEM and TEM images of the as-synthesized Ti_1/rGO samples, respectively. It can be clearly observed that the Ti_1/rGO appears as an ultrathin, wrinkled and interlaced sheet, similar to the rGO sample (Supplementary Fig. 4), which suggests that both Ti_1/rGO and rGO samples retain the excellent flexibility of graphene[14]. The selected area electron diffraction (SAED) pattern (the inset of Fig. 1c) reveals that the Ti_1/rGO sample mainly

consists of ~~the diffraction information of~~ layered graphene. In the TEM measurement, the energy-dispersive X-ray (EDX) mapping of Ti_1/rGO was also performed on a small region. The

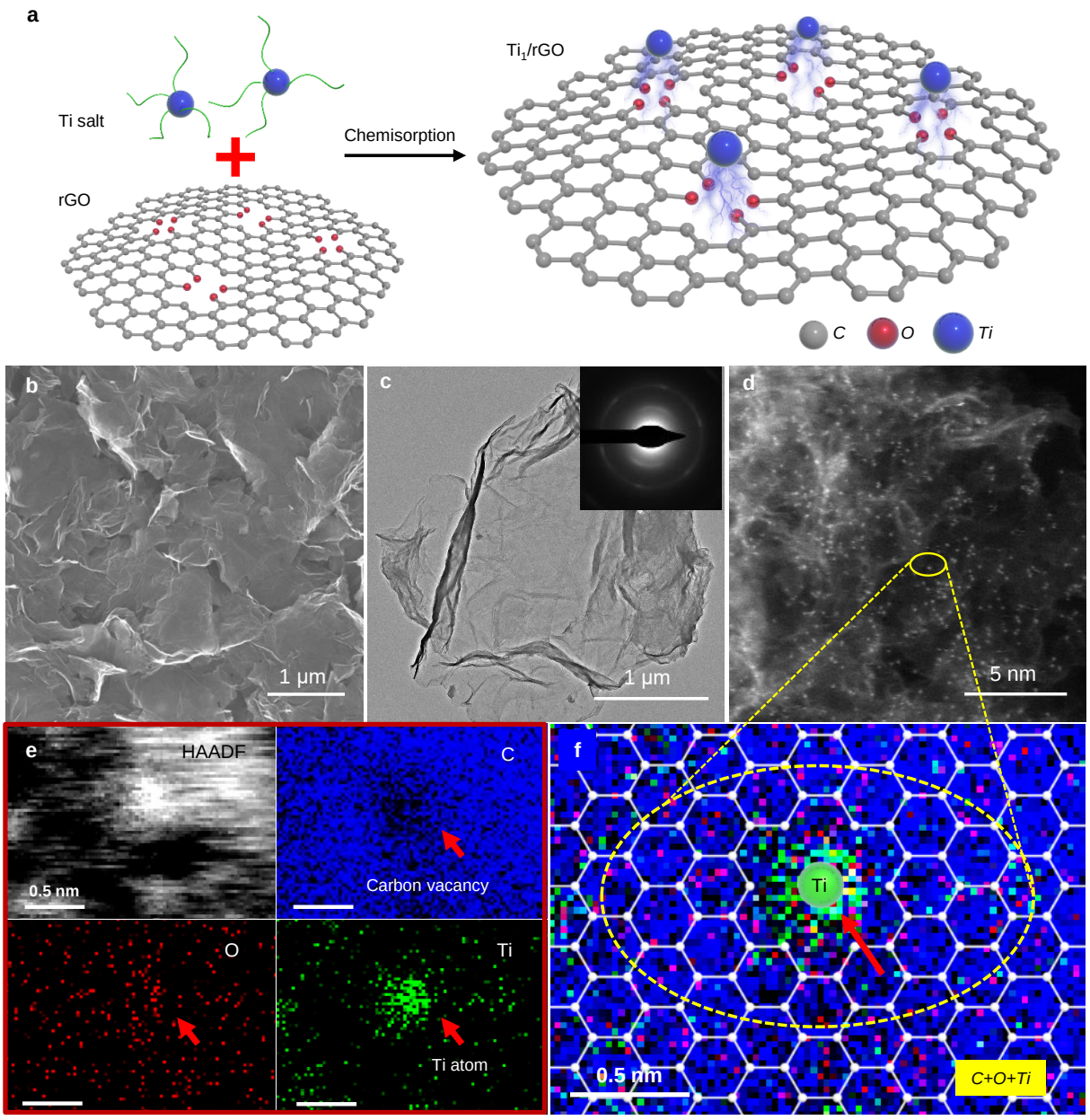

Fig. 1 | Structural characterizations of Ti_1/rGO. a, Schematic illustration of the synthesis of Ti_1/rGO. **b, c,** SEM (**b**) and TEM (**c**) images of Ti_1/rGO. The inset in TEM image is the selected area electron diffraction (SAED) of Ti_1/rGO. **d,** High-angle annular dark field scanning transmission electron microscopy (HAADF-STEM) image of Ti_1/rGO. **e,** HAADF image and electron energy loss spectroscopy (EELS) map of C, O and Ti elements of Ti_1/rGO. **f,** EELS color-coded map of C, O, Ti of Ti_1/rGO. The overlaid schematic represents a possible structural model of Ti_1/rGO around a Ti atom determined from EELS overlap mapping image analysis.

EDX mapping of C, O, and Ti confirms that these elements are uniformly distributed across the entire sample (Supplementary Fig. 5). Subsequently, the dispersion of Ti atoms on the rGO was confirmed by the high-angle annular dark field scanning transmission electron microscopy (HAADF-STEM). The bright spots in HAADF-STEM image (Fig. 1d) correspond to Ti atoms and are homogeneously distributed throughout the entire Ti_1/rGO sample. All the above analyses indicate the successful synthesis of rGO-supported single Ti-atom material.

To circumvent the limited discrimination ability of the HAADF signal, electron energy loss spectroscopy (EELS) was employed with simultaneous HAADF signal to investigate the local bonding of individual Ti atom[32]. The EELS mapping of Ti_1/rGO was acquired on a region around the center of one isolated Ti atom from the large-area HADDF image. As presented in Fig. 1e, it is apparent that the position of Ti atom (as depicted by the red arrow in the Ti-$L_{2,3}$ EELS map) corresponds exactly to that of the carbon vacancy (the red arrow in the C-*K* EELS map), which evidences that the Ti adatom is anchored into a carbon-vacancy defect of Ti_1/rGO SAM. Besides, O distribution in the EELS map appears slightly gathered around the Ti atom, which implies that the Ti atom most likely coordinates with oxygen atoms on rGO directly. Furthermore, the respective EELS spectrum for C, O and Ti elements around the Ti atom center (as shown by the red arrow in Fig. 1f) demonstrates the presence of C and O signals, indicative of the formation of Ti-O-C bonding (Supplementary Fig. 6).

Coordination structure of Ti atom in Ti_1/rGO

The synchrotron-radiation-based X-ray absorption near-edge structure (XANES) and extended X-ray absorption fine structure (EXAFS) spectroscopy are utilized to further identify the coordination structure concerning Ti atom in Ti_1/rGO [33]. As presented in Fig. 2a, the Ti K-edge XANES spectra show that the absorption edge energy of Ti_1/rGO lies between that of TiC and TiO_2, corroborating that the oxidation state of Ti species in Ti_1/rGO is about +4, which is further supported by X-ray photoelectron spectroscopy (XPS) and XANES analysis

(Supplementary Note 1, Supplementary Fig. 7 and Supplementary Table 2). Through the established metal oxidation vs. E_0 relationship, the Ti average valence state in the Ti_1/rGO sample is estimated to be ~ + 3.70 (Supplementary Fig. 7d). Quantitative evidence on the bonding characteristics of the Ti atoms in Ti_1/rGO can be further revealed through the EXAFS spectroscopy analysis. The Fourier-transformed (FT) k^2-weighted $\chi(k)$ EXAFS spectrum of Ti_1/rGO in Fig. 2b demonstrate that the main peak located at $R \approx 1.44$ Å is close to that of TiO_2 reference, which can be ascribed to the Ti-O/C coordination. Besides, the co-presence of well-separated FT peak at $R \approx 2.42$ Å much resembles those of pyridine or pyrrolic N atoms coordinated M-N_4 moiety in the previously reported M-N-C SAMs [34,35]. To interpret, we considered two separate Ti-O/C_1 and Ti-C_2 scattering paths. Based on the quantitative EXAFS curve fitting analysis (Figs. 2c-d and Supplementary Table 2), the average Ti environment within Ti_1/rGO comprises first-shell Ti-O (coordination number $N = 4.9 \pm 0.4$, $R = 1.94 \pm 0.02$ Å) and second shell Ti-C ($N = 3.5 \pm 0.6$, $R = 3.00 \pm 0.04$ Å). Considering the difficulties of EXAFS analysis in discriminating the C/O neighbors and the definite structural configuration, XANES simulations and DFT calculations on Bader charge analysis were further carried out to precisely interpret the definite atomic-site $Ti_1O_xC_y$ structure (Supplementary Note 2, Supplementary Figs. 8-10, Supplementary Table 4). By contrast, the TiO_4-OH can better reproduce the main features and give a relatively closer match with the experimental spectrum (Fig. 2e), which is also supported by subsequent Bader charge analysis (Fig. 2f). Specifically, the calculated Ti valence state (+3.82) of proposed TiO_4-OH is much closer to that (+3.70) derived from the XANES analyses. On the other hand, the coordination number $N_{Ti\text{-}C} = 3.5$ at the second shell is slightly lower than that (N = 4.0) of the theoretically predicted structure, which could be due to the large structural disorder in our case or defects. As far as we concerned, this underestimation for $N_{second\text{-}shell}$ of photo-absorber is also often encountered in EXAFS fitting analysis of SAMs [34,36]. By virtue of combined theoretical and experimental study, our findings

nonetheless indicate that isolated TiO_4-OH moiety species were dominantly formed on the rGO support. By consulting the aforementioned EELS results, we therefore conjecture the formation of such a specific moiety is because Ti adatoms can be anchored by oxygen atoms at rGO vacancy defect.

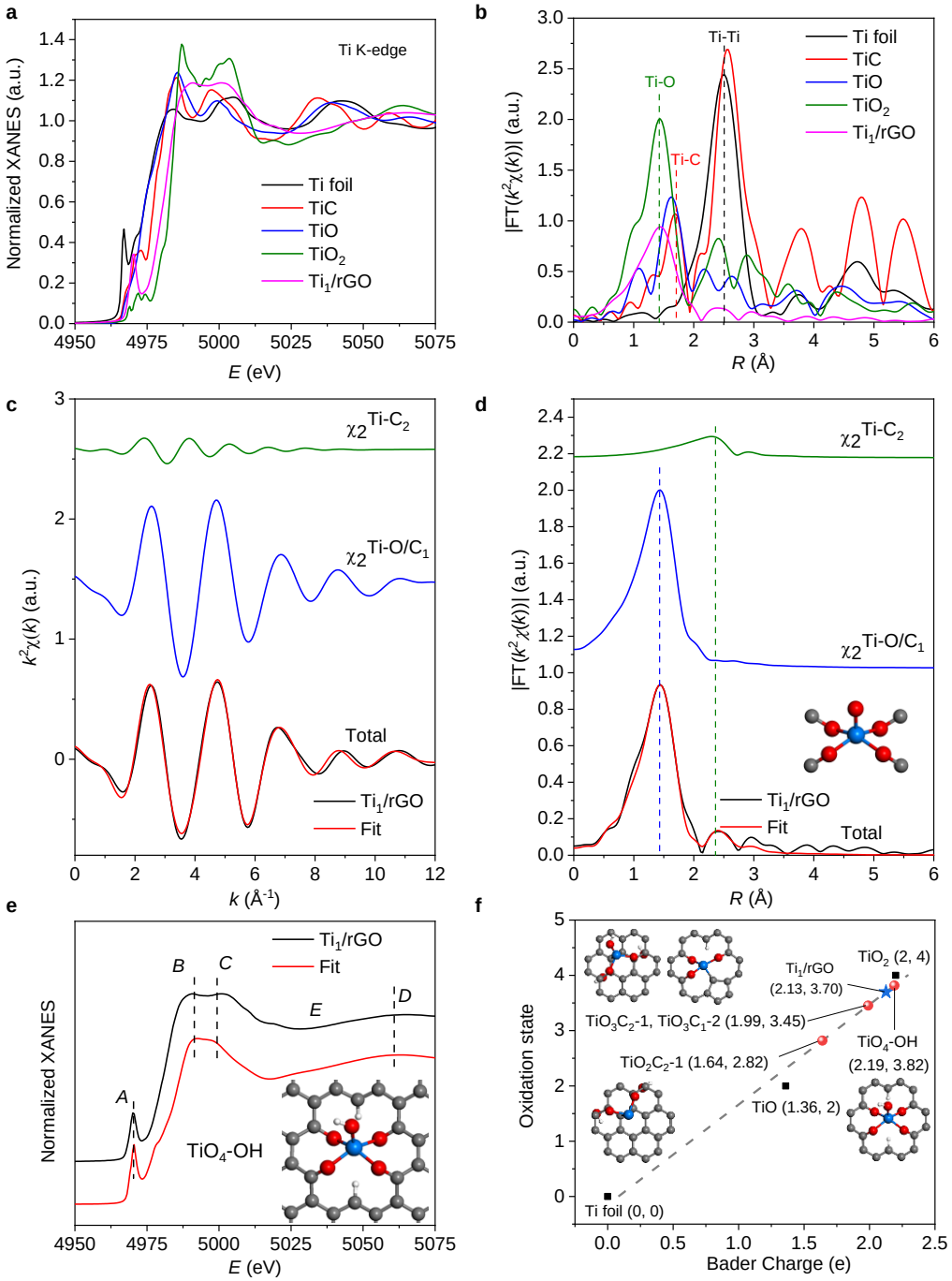

Fig. 2 | Coordination structure analysis of Ti atom in Ti_1/rGO. a,b, Normalized Ti K edge X-ray absorption near edge structure (XANES) spectra (**a**) and radial distance (*R*) space spectra (**b**) of Ti_1/rGO and the Ti foil, TiC, TiO_2 as reference respectively. **c,d,** Ti K-edge EXAFS analysis of Ti_1/rGO in *k* (**c**)

and *R* (**d**) spaces. Curves from top to bottom are the Ti-C and Ti-O two-body backscattering signals χ_2 included in the fit and the total signal superimposed on the experimental signal (black line). The measured and calculated spectra show excellent agreement. The inset in d shows the structure of a Ti_1-O_5-C_4 moiety originating from the EXAFS result, where the blue, red, grey spheres represent Ti, O and C, respectively. **e**, Comparison between the K-edge XANES experimental spectrum of Ti_1/rGO and the theoretical spectrum calculated based on Ti_1-O_4-OH moieties embedded in the graphene lattice. The inset in e shows the most possible configuration of Ti_1/rGO, where the blue, red, grey, white spheres represent Ti, O, C and H, respectively. **f,** The fitted average oxidation states of Ti in TiO_3C_2-1, TiO_3C_1-2, TiO_2C_2-2 and TiO_4-OH structural models, where the blue, red, grey, white spheres represent Ti, O, C and H, respectively. Bader charges of Ti foil, TiO and TiO_2 are linearly fitted with their oxidation states, which are known as 0, +2 and +4, respectively.

Electronic properties of Ti_1/rGO electrode

Firstly, the influence of introducing atomic titanium on the electrical property of the rGO electrode was theoretically investigated through DFT calculation. As displayed in Fig. 3a, the energy band structure based on a rGO structure model (inset of in Fig. 3a) shows a band gap of 0.3 eV (energy bands are discontinuous near the Fermi level) leading to non-metallic behavior, which is disadvantageous for the conductivity. Fortunately, there is a shift of the Fermi level into the valence band for Ti_1/rGO (Fig. 3b) leading to a metallic behavior and, concomitantly, to better conductivity. ~~The improvement of Ti/rGO conductivity is well confirmed by the linear sweep voltammetry (LSV) characteristics in based on the sandwich symmetric structure cell (FTO/graphene/FTO) shown in Supplementary Fig. 11.~~ The electrostatic potential along the Z-axis and detailed parameter calculated for rGO and Ti_1/rGO in Fig. 3c-d and Supplementary Table 5 predict that the Ti single atom loaded on rGO will lead to a substantially increase in the work function (W_F) from 4.04 eV (rGO) to 4.79 eV (Ti_1/rGO).

Based on the ultraviolet photoelectron spectrometer (UPS) in Fig. 3e and detailed calculations of the W_F provided in Supplementary Fig. 11, the Fermi levels (E_F) of rGO, Ti_1/rGO and spiro-OMeTAD are estimated to be -4.05 eV, -4.31 eV and -4.25 eV, respectively. As shown in Fig. 3f, the Fermi levels of rGO and Spiro-OMeTAD show an energy mis-alignment of 200 meV which could result in a V_{oc} loss whereas those of Ti_1/rGO and spiro-OMeTAD are well aligned

avoiding any significant voltage loss during interfacial hole transfer from spiro-OMeTAD to Ti_1/rGO.

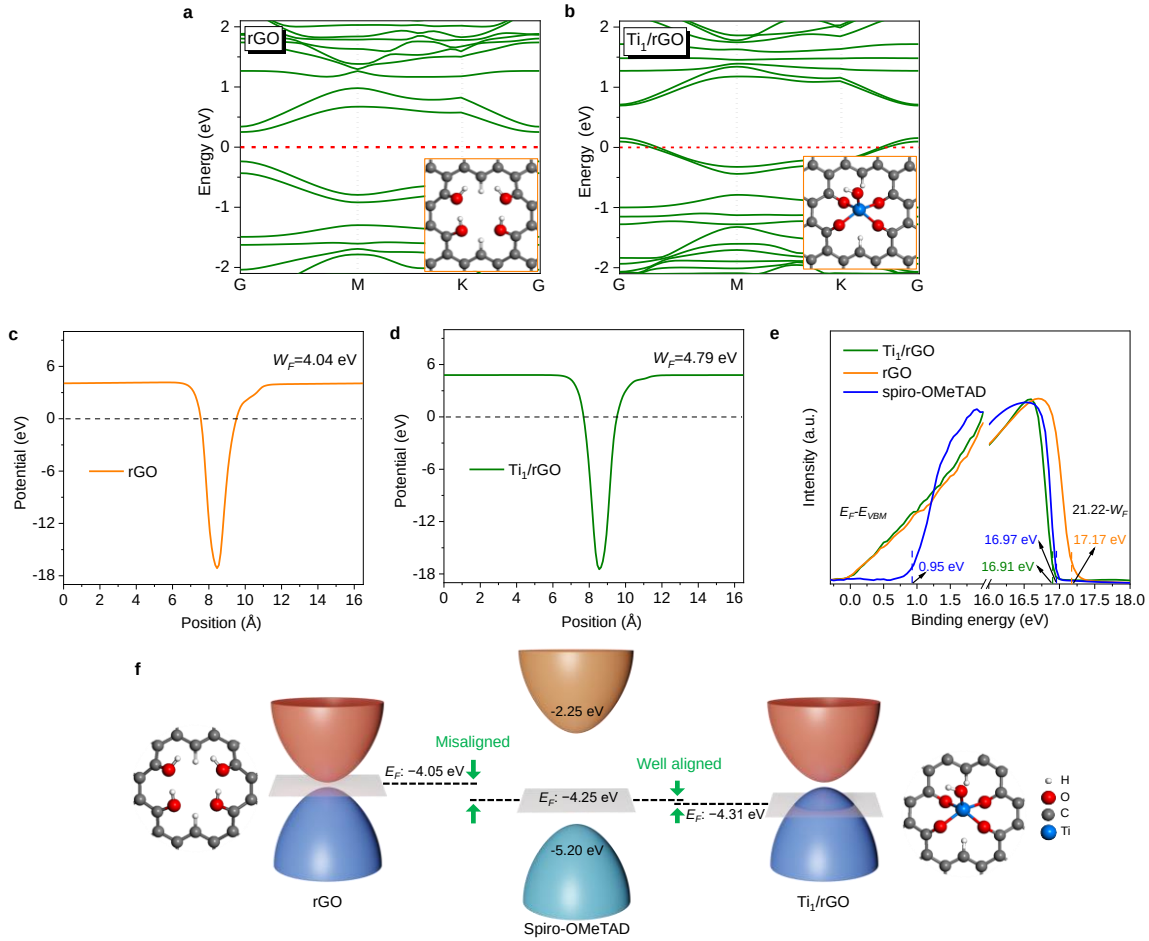

Fig. 3 | Mechanistical insight into tuning the electric properties of Ti_1/rGO electrode. a,b, The theoretically calculated energy band structure based on the chemical structure model of rGO (**a**) and Ti_1/rGO (**b**) in the corresponding inset, respectively. The Fermi energy is set at 0 eV. ~~c, Linear sweep voltammetry (LSV) characteristics of three FTO/rGO/FTO and three FTO/(Ti_1/rGO)/FTO samples (with the same graphene thickness).~~ **c, d,** The electrostatic potential along Z-axis for rGO (**c**) and Ti_1/rGO (**d**). **e,** UPS spectra of Spiro-OMeTAD, rGO and Ti_1/rGO. **f,** The schematic band alignment of between spiro-OMeTAD and electrode materials.

Performance and stability of Ti_1/rGO-based C-PSCs

The various improved electrical properties of Ti_1/rGO motivate us to scrutinize whether the improvement in basis properties of Ti_1/rGO electrode material can be translated into performance enhancement of the entire C-PSCs device. To this end, we employed rGO and Ti_1/rGO as the electrode materials of modular C-PSC with advanced architecture, respectively,

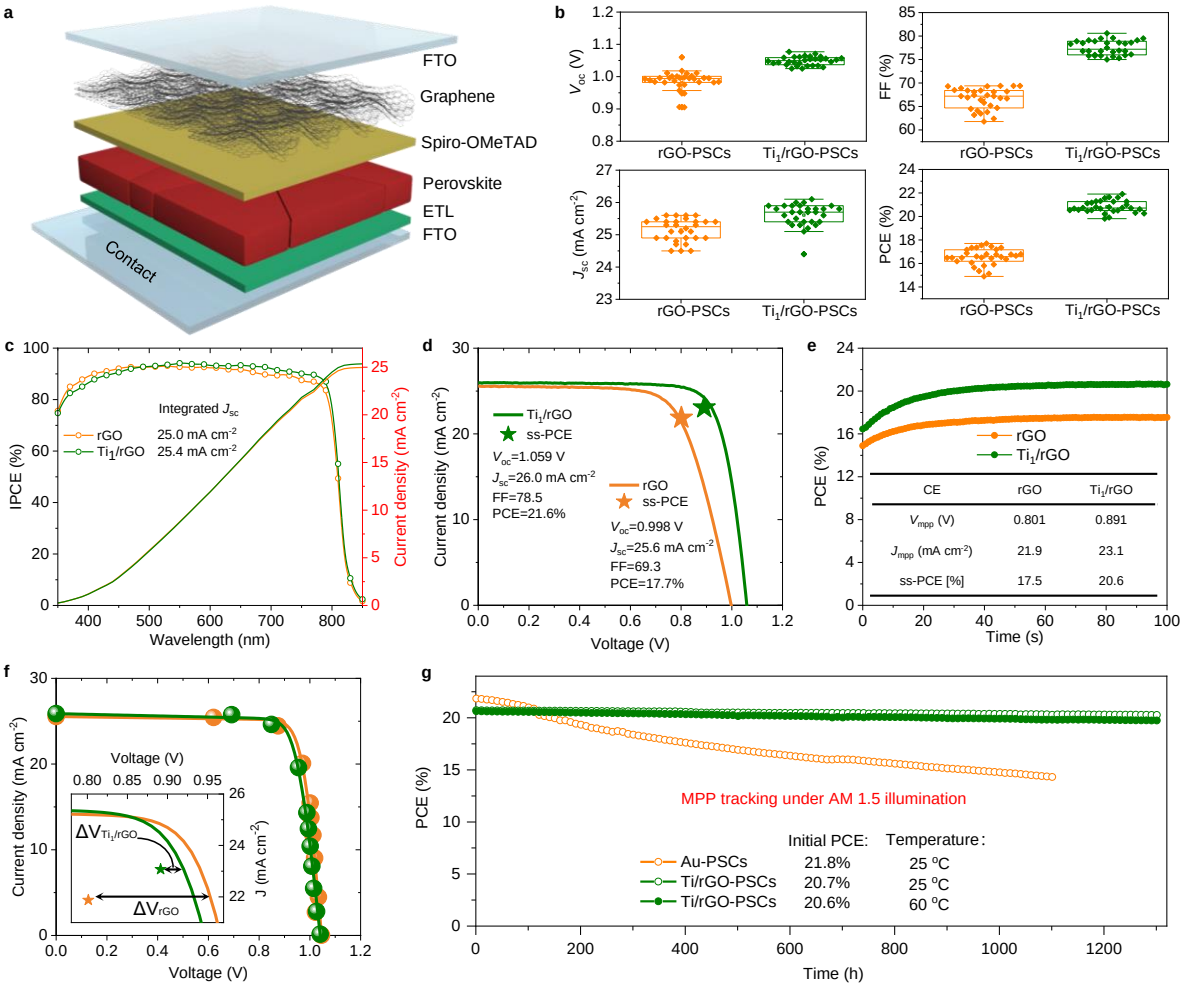

Fig. 4 | Photovoltaic performance and operational stability. a, Schematic diagram of modular C-PSC structure, which is assemed by stacking semi-cell A (FTO/ETL/perovskite/spiro-OMeTAD/graphene) and charge collector B (FTO/graphene). **b,** The statistics of photoelectric performance parameters (V_{oc}, J_{sc}, FF, PCE) distribution for 60 devices with the architecture FTO/c-TiO_2/mp-TiO_2/perovskite$_1$/spiro-OMeTAD/rGO or Ti_1/rGO (30 Ti_1/rGO-based C-PSCs and 30 rGO-based C-PSCs). The box plot denotes median (centre line), 75th (top edge of the box), 25th (bottom edge of the box). The solid dots represent original data. All these performance parameters were obtained on the reverse scan. **c,** IPCE spectrum and the integrated photocurrent density of the rGO-based C-PSC and Ti_1/rGO-based C-PSC. **d,** *J-V* curve (reverse sweep rate: 125 mV/s) of the rGO (orange) and the Ti_1/rGO (green) devices. The stars indicate the steady-state maximum power point (ss-MPP) of the two devices. **e,** The steady-state PCE (ss-PCE) of rGO-based C-PSC and Ti_1/rGO-based C-PSC, inset shows the ss-MPP parameters devices of rGO-based C-PSC and Ti_1/rGO-based C-PSC. **f,** Steady-state J_{sc}-V_{oc} measurements (circles) and fit curves for the same devices as in (**d**). The inset shows the J_{sc}-V_{oc} fit curves in a magnified scale along with the ss-MPP measurements. **g,** MPP ageing of Ti_1/rGO-based C-PSC (25 °C and 60 °C, respectively) and conventional thermal evaporation Au-PSC (25 °C) under N_2 atmosphere, 1 sun continuous illumination.

Table 1 | Photovoltaic parameters of C-PSCs with the architecture FTO/c-TiO_2/mp-TiO_2/perovskite$_1$/spiro-OMeTAD/rGO or Ti_1/rGO.

Sample	V_{oc} [V]	J_{sc}[mA cm^{-2}]	FF [%]	PCE [%]
Champion	0.998	25.6	69.3	17.7

rGO	Average	0.988±0.030	25.1±0.4	66.7±2.3	16.6±0.7
Ti_1/rGO	Champion	1.059	26.0	78.5	21.6
	Average	1.049±0.014	25.6±0.3	77.5±1.6	20.8±0.5

which were assembled through stacking a semi-cell A (FTO/ETL/perovskite/spiro-OMeTAD/graphene) and charge collector B (FTO/graphene) with very a small mechanical pressure (around 4.7 kPa, Supplementary Figs. 13 and 14). Such an architecture has been proven to possess numerous advantages, such as being easily assembled, disassembled, repaired and upgraded, etc[14]. The modular C-PSCs structure diagram is illustrated in Fig. 4a.

Firstly, we applied the rGO and Ti_1/rGO contact layers to perovskite solar cell with the architecture using high-temperature processed TiO_2 as ETL and $Cs_{0.05}FA_{0.85}MA_{0.10}Pb(I_{0.97}Br_{0.03})_3$ as perovskite layer (labeled as perovskite$_1$)[37]. The performance parameters distribution statistics of devices with the architecture FTO/c-TiO_2/mp-TiO_2/perovskite$_1$/spiro-OMeTAD/rGO or Ti_1/rGO are shown in Fig. 4b, and the average parameters of 60 devices were summarized in Table 1. Evidently, the average PCE of the devices soars from 16.6% (rGO-based C-PSCs) to 20.8% upon applying Ti_1/rGO. Further, the Ti_1/rGO-based C-PSC affords an encouragingly high J_{sc} of up to 26.0 mA cm^{-2}, which is in good agreement with the integrated current density (25.4 mA cm^{-2}) originating from the incident photon-to-electron conversion efficiency (IPCE) spectra (Fig. 4c). Meanwhile, the narrow PCE distribution for Ti_1/rGO-based C-PSCs suggests a better reproducibility in comparison to control rGO-based C-PSCs.

Fig. 4d shows the IV curve of champion Ti_1/rGO-based C-PSC with an open-circuit voltage (V_{oc}) of 1.059 V, a short-circuit current density (J_{sc}) of 26.0 mA cm^{-2}, a fill factor (FF) of 78.5% and a PCE of 21.6%, which surpasses that of champion rGO-based C-PSC (17.7%) and is closer to the PCE (23.5%) of Au-PSCs (Supplementary Fig. 14). Note that the Ti_1/rGO-based C-PSC presents an elevated FF of up to 78.5%, in comparison to 69.3% for the control rGO-based C-

PSC, as a result of the improved electrical properties of Ti_1/rGO as we show further below. To exclude hysteresis effects in the PCE determination we measured the steady-state (ss) MPPs, i.e., a time-dependent MPP measurement has been carried out until the MPP stabilized (Fig. 4e). The detailed parameters of the ss-MPPs can be found in inset of Fig. 4e. For the rGO device we obtained a stabilized PCE of 17.5% and for the Ti_1/rGO device 20.6%. To our knowledge the latter is the highest PCE to date for a C-PSC.

To evaluate the reason behind the device performance difference of rGO and Ti_1/rGO based perovskite solar cells we performed J_{sc}-V_{oc} measurements, which have been used to determine the series resistance of solar cell devices[38,39]. Fig. 4f shows the J_{sc}-V_{oc} curves of the rGO and Ti_1/rGO devices. The J_{sc}-V_{oc} curves of both devices are nearly the same, which indicates that the main performance difference between the two devices comes from a different series resistance. To illustrate this further, we depict the reverse sweep *J*-*V* curves and the J_{sc}-V_{oc} curves (Supplementary Fig. 15). For the rGO device the *J*-*V* sweeps deviate significantly from the J_{sc}-V_{oc} traces whereas for Ti_1/rGO they nearly overlap. To quantify this behavior, we calculate the series resistance at MPP. With the voltage difference ΔV between V_{MPP} and the J_{sc}-V_{oc} curve at J_{MPP} (inset of Fig. 4f) the series resistance at MPP is $R_s(MPP) = \Delta V / J_{MPP}$. For the rGO device the series resistance is 7.0 Ω cm^2 and for the Ti_1/rGO device 1.3 Ω cm^2. This shows that the series resistance of the rGO layer is significantly larger than that of the Ti_1/rGO layer and this is the main reason for the performance difference.

To verify the universality of carbon electrode in different perovskite cell architectures, we also applied the rGO and Ti_1/rGO contact layers to another perovskite solar cell architecture using low-temperature processed SnO_2 as ETL and classical $Cs_{0.05}[(FAPbI_3)_{0.85}(MAPbBr_3)_{0.15}]_{0.95}$ as perovskite layer (labeled as perovskite$_2$) [40]. The device architecture is FTO/SnO_2/perovskite$_2$/spiro-OMeTAD/rGO or Ti_1/rGO. A high PCE up to 19.8% is achieved by our Ti_1/rGO-based device, evidently higher than that (16.8%) of the control

device based on the bare rGO (Supplementary Note 4, Supplementary Figs. 16 and 17, Supplementary Table 6). Those results are similar to that of the device with TiO_2 as ETL, which further demonstrates the wide application of Ti_1/rGO as high-performance electrode materials. Here, an important fact worth noting is that the hole transport layer (HTL), such as spiro-OMeTAD used in our C-PSCs, is indispensable to minimize charge recombination. We fabricated Ti_1/rGO-based and rGO-based HTL-free C-PSCs (see detail results and analysis in Supplementary Fig. 18, Supplementary Table 7 and Supplementary Note 5). The PCEs of both Ti_1/rGO-based and rGO-based HTL-free device are evidently inferior to that of the one containing HTL due to a major loss in FF and V_{oc}. This can be ascribed to the metallic nature of Ti_1/rGO or rGO due to which the hole-extraction is not as selective as that in the case using HTL, and the back-transfer of electron cannot be blocked effectively, in turn leading to serious charge recombination at the (Ti_1/rGO)/perovskite or rGO/perovskite interface. Therefore, HTL is thought to be essential to achieve high efficiency C-PSCs. In addition, as shown in Supplementary Fig. 19, the device using cheap Al foil as substrate in charge collector B still realized a high PCE up to 20.9%, endowing many options available in terms of the conductive substrate in charge collector B, and favorable to further reducing production cost.

Furthermore, in terms of an exceptional electrode material, stability of Ti_1/rGO is also our focus. The operational stability data obtained with Ti_1/rGO-based C-PSCs and conventional thermal evaporation Au-based PSCs (Au-PSCs) at MPP under the same condition (1 sun irradiation and in N_2 atmosphere) were measured to reflect the stability of the electrode materials. As illustrated in Fig. 4g and Supplementary Fig. 20, the PCE at MPP of Au-PSC rapidly decayed from 21.8% to 14.3% after 1100 h continuous irradiation at 25 ^oC, with only 65% of initial value being retained. By contrast, the operational stability of Ti_1/rGO-based C-PSC without encapsulation is excellent while its PCE at MPP can maintain 98% (20.2%) of its initial value (20.7%) after continuous irradiation for 1300 h at 25 ^oC. Even at 60 ^oC, the PCE at

MPP of Ti1/rGO-based C-PSC can maintain 95% (19.7%) of its initial value (20.6%) after continuous irradiation for 1300 h. Therefore, we believe that Ti_1/rGO is an excellent candidate to address the instability issue caused by the corrosion of the precious metal electrode.

Conclusions

In summary, we report the application of SAM with a well-defined structure as back contact for high performance perovskite solar cells. DFT calculations indicate the evident charge transfer between rGO and Ti adatoms, which leads to a substantially improved conductivity of the Ti_1/rGO charge transport material. As expected, by combination with an advanced modular cell architecture, a steady state PCE of up to 20.6% is achieved based on this unique back contact material. Moreover, the Ti_1/rGO-based C-PSC without encapsulation displays an excellent stability while its MPP tracking under in full sun still retain 98% and 95% of their initial values for 1300 h (1-sun, in N_2 atmosphere) at 25 ^oC and 60 ^oC, respectively. This work not only provides a novel avenue to engineer efficient and stable electrode materials for C-PSCs, but also deepens the understanding of the correlation between electronic device properties and chemical structure.

Methods

Materials. FTO (7 Ω sq^{-1}) was purchased from Yingkou OPV Tech New Energy Co., Ltd. CsI (99.999%), 4-tert-butylpyridine (TBP, 96%), bis(trifluoromethane)sulfonimide lithium salt (Li-TFSI, 99.95%), isopropanol (99.5%), dimethyl sulfoxide (DMSO, 99.9%), dimethylformamide (DMF, 99.8%), acetonitrile (99.8%), chlorobenzene (CB, 99.8%), α, α, α-trifluorotoluene (≥99%), acetyl acetone, phenethylamine and titanium diisopropoxide bis(acetylacetonate), 75 weight % in IPA were obtained from Sigma Aldrich. $SnCl_2$ $2H_2O$ (98%) was provided from Alfa Aesar. CH_3NH_3Br (MABr) and $CH(NH_2)_2I$ (FAI) were received from Xi'an Polymer Light Technology Corp. PbI_2 (99.99%), $PbBr_2$ (>98.0%) were ordered from TCI. Spiro-OMeTAD (99.7%) was supplied by Lumtec. Ethanol and acetone were bought from Sinopharm Chemical Reagent Co., Ltd. Graphite oxide (SE2430) was purchased from The Sixth Element Materials Technology Co., Ltd.

Preparation of Ti_1/rGO and rGO. The Ti_1/rGO SAM sample was prepared via chemisorption route. First, 400 mg of graphite oxide was dispersed into 120 mL of isopropanol. Then, 20 μL of organic Ti salt (titanium

diisopropoxide bis(acetylacetonate)) was added into the above solution with continuous magnetic stirring, followed by ultrasonic dispersion for 1h and magnetic stirring for 20 h. Afterward, the above dispersion solution was centrifuged and the resulting precipitation was dried at 85 °C in vacuum for 24 h. Thereafter, the obtained powder was calcinated at 550 °C for 2 h in a high purity N_2 atmosphere. After cooling to room temperature, the fluffy black powder was Ti_1/rGO SAM. Likewise, rGO could be obtained through the same steps without adding organic Ti salt.

Fabrication of modular C-PSCs. 10 mg of carbon material (rGO or Ti_1/rGO) was dispersed into 20 ml of isopropanol solution, followed by ball-milling for 12 h. The dispersion slurry for spraying was obtained. FTO glasses were etched with zinc powder and 4 M HCl, rinsed with cleaning fluid, deionized water, ethanol, acetone and isopropanol, respectively.

Fabrication of architecture FTO/c-TiO_2/mp-TiO_2/perovskite$_1$: When the FTO glass was preheated to 450 ℃, the compact TiO_2 layer was deposited on the FTO glass through spray pyrolysis method (the carrier gas is O_2). The precursor solution of the compact TiO_2 layer (c-TiO_2) was diluted 600 μL titaniumdiisopropoxide bis(acetylacetonate) and 400 μL acetyl acetone with 9 mL ethanol. After spray pyrolysis, the FTO/c-TiO_2 was sinter at 450 ℃ for 10 min before cooling down to room temperature. After that, mesoporous TiO_2 (mp-TiO_2) was deposited on the c-TiO_2 layer through spin-coating for 20s at 4000 rpm. The precursor solution of m-TiO_2 was diluted the commercial TiO_2 paste (30NRD, Dyesol) with ethanol at a weight ratio of 1:6. The FTO/c-TiO_2/mp-TiO_2 was heated at 450 ℃ for 30 min under dry air flow. To deposit the perovskite layer, one-step spin-coating method was adopted to prepare the $Cs_{0.05}FA_{0.85}MA_{0.10}Pb(I_{0.97}Br_{0.03})_3$ perovskite layer with 5% excess of PbI_2 in 1 mL mixed solvent of DMF and DMSO (4:1 volume ratio). Subsequently, 120 μL of perovskite solution was spin coated on the ETL via a two-step spin coating program with 2000 rpm for 10 s with an acceleration rate of 200 rpm/s and 6000 rpm for 30 s with an acceleration rate of 2000 rpm/s, respectively. Then 300 μl of anti-solvent (CB) was dropped on the spinning substrates 15 s prior the end of program, followed by annealing at 120 °C for 20 min.

Fabrication of architecture FTO/SnO_2/perovskite$_2$: The 0.1 M $SnCl_2$ $2H_2O$ isopropanol solution was refluxed at 85 °C for 3 h to obtain the SnO_2 sol for electron extraction layer (ETL) of PSCs. The prepared precursor was spin-coated on the FTO glass at 2000 rpm for 30 s, followed by thermal treatment at 80 °C for 1 h in the air. After that, the as-deposited SnO_2 ETL was treated with UV-Ozoneor 20 min. To deposit the perovskite layer, one-step spin-coating method was adopted to prepare the $Cs_{0.05}[(FAPbI_3)_{0.85}(MAPbBr_3)_{0.15}]_{0.95}$ perovskite layer. Typically, FAI (1 M), PbI_2 (1.1 M), MABr (0.2 M) and $PbBr_2$ (0.2 M) were dissolved in 1 mL mixed solvent of DMF and DMSO (4:1 volume ratio), and then stirred at 60 °C for 2 h. Next, 1 M CsI DMSO solution was added to the above perovskite precursor solution with a volume ratio of 5:95. Subsequently, 120 μL of perovskite solution was spin coated on the ETL via a two-step spin coating program with 1000 rpm for 10 s and 6000 rpm for 30 s, respectively. Then 300 μl of anti-solvent (α, α, α-trifluorotoluene) was dropped on the spinning substrates 20 s prior the end of program, followed by annealing at 85 °C for 45 min.

The spiro-OMeTAD precursor solution was obtained via adding 72.3 mg of spiro-OMeTAD powder, 29 μL of TBP, 17.5 μL of Li-TFSI acetonitrile solution (520 mg/mL) into chlorobenzene (1 mL). Afterward, 50

μL of the spiro-OMeTAD solution was spin coated on the above perovskite films at 3000 rpm for 30 s. The semi-cell was obtained successfully. Then 500 μL of carbon slurry based on rGO or Ti_1/rGO was sprayed on the above semi-cells (FTO/ETL/perovskite/HTL) and FTO substrates on a hotplate at 85 °C to accelerate solvent evaporation. The obtained semi-cell A (FTO/ETL/perovskite/HTL/carbon) and charge collector B (FTO/carbon) were then assembled into modular C-PSC by being stacked together using retaining clips, and the overall thickness of graphene on two carbon electrodes was compressed to about 2 μm.

Characterizations. The STEM images of Ti_1/rGO SAM sample were acquired using a STEM (JEOL ARM-200F) equipped with an aberration corrector (CEOS CESCOR) at the probe side, which was operated at the accelerating voltage of 80 kV. The dwell time per pixel was set to 10-16 us. The morphologies of samples were characterized by scanning electron microscopy (SEM, SU8220, JAPAN) and scanning transmission electron microscope (TEM, F-20, FEI, Netherlands). ~~The X-ray absorption spectra (such as X-ray absorption near-edge structure (XANES) and extended X-ray absorption fine structure (EXAFS) spectra) were monitored by BL14W1 of the Shanghai Synchrotron Radiation Facility (SSRF), China.~~ A double Si (111)-crystal monochromator was adopted for energy selection. The energy was calibrated by the Ti foil. ~~The spectra were recorded under the transmission mode at room temperature. The XANES data were processed through Athena software.~~ *J-V* characteristics of modular C-PSCs were conducted on a digital source meter (Keithley 2450) at the scan speed of 100 mV s^{-1}. The simulated AM 1.5G sunlight (irradiance equivalent to 100 mW cm^{-2}) calibrated by standards Si reference cell (Si photodiode (FDS1010-CAL from Thorlabs) with KG5 filter, calibrated by Newport.) was generated through a solar simulator (Newport Sol 3A). We continuously verify our measurements with PV certification labs (Fraunhofer ISE, Newport). The modular C-PSCs were masked through a black metal mask with an aperture area of 0.09 cm^2 during *J-V* measurement. The stable output of photocurrent and PCE were detected with a digital source meter (Keithley 2450) at a certain bias. The incident photon-to-electron conversion efficiency (IPCE) spectra was performed using a commercial apparatus (Aekeo-Ariadne, Cicci Research s.r.l.) with a 300 W Xenon lamp. Stability of the cells were recorded under a white light-emitting diode lamp with biologic MPG2 potentiostat and N_2 atmosphere. The spectral mismatch between AM 1.5G and the simulated sunlight was calibrated with a Schott K113 Tempax filter.

STEM-EELS measurements and data analysis: The Ti_1/rGO powder was uniformly dispersed by sonication in high-purity ethanol, then the solution was dropped onto a 400-mesh lacey-carbon gold grid for the electron energy-loss spectroscopy mapping in the scanning transmission electron microscopy mode (STEM-EELS). Before the STEM-EELS measurements, the grid was annealed at 100°C in a high vacuum chamber of ~10^{-6} mbar for overnight to completely remove the ethanol residual as well as any adsorbed vapor. The JEOL JEM ARM-200F equipped with the cold field-emission gun and the ASCOR fifth-order probe-side corrector was applied for the STEM-EELS experiments under 60 kV accelerating voltage to avoid sample damage. The 30 mrad convergence semi angle and ~120 pA probe current were selected for the optimized information transfer and single-atom sensitivity[41]. An energy dispersion of 0.25 eV per channel and 91 mrad collection semi angle in the Gatan Enfinium ER spectrometer were set up with corrected stigmatism up to the third order. Each STEM-EELS map was acquired using 1 ms dwell time (near 1000

spectra per second) and 0.25 Å pixel size to maintain relatively low electron dose. The zero-loss peak and core-loss edges were simultaneously recorded for the absolute energy scale. The simultaneous annual dark field (ADF) signal was acquired using a 93 mrad inner collection semi angle. The signal-to-noise ratio of single-pixel spectrum in the STEM-EELS dataset under as-described experimental conditions is low but adequate to distinguish the Ti L_3 and L_2 edges (fine structures visible when averaged across the whole sampled region). The spectrum background was subtracted using the method of local background averaging and linear combination of two power laws to benefit from the redundant sampling[42]. Instead of the direct integration of the Ti edges, principal component analysis (PCA) was first performed to search for the reference spectrum of Ti_1, then the non-negative least-square fitting of the spectra dataset by the reference spectrum generates the Ti concentration map of enormously improved contrast.

XAFS measurements and data analysis. The Ti K-edge X-ray absorption fine structure (XAFS) spectra were collected at BL11B beamline in Shanghai Synchrotron Radiation Facility (SSRF), China. The hard X-ray was monochromatized with Si(111) double-crystal monochromator and the harmonic rejection mirror was used to remove monochromator harmonics. The as-prepared Ti_1/rGO sample was first pelletized as disk of 10 mm and the XAFS data were collected in fluorescence mode (Lytle detector) in the energy range from -200 below to 800 eV above the Ti K-edge. The acquired EXAFS data were processed according to the standard procedures using the ATHENA module implemented in the IFEFFIT software packages[43]. The $k^2\chi(k)$ weighted data in the k-space ranging from 2.0-11.5 $Å^{-1}$ were Fourier transformed to real (R) space using a hanning windows (dk =1.0 $Å^{-1}$) to separate the EXAFS contributions from different coordination shells. The EXAFS curve-fittings were performed using the ARTEMIS module of IFEFFIT [44]. Effective backscattering amplitudes $F(k)$ and phase shifts $\Phi(k)$ of all fitting paths were calculated with the ab initio code FEFF8.0[45]. Fittings were done in the R-space within the R-range of [1.0, 2.7] Å for k^2-weighted $\chi(k)$ functions with Hanning windows (dk =1.0 $Å^{-1}$), and the number of independent points $N_{ipt} = 2\triangle k\triangle R/\pi$ $=2\times(11.5-2)\times(2.7-1)/\pi = 10$. During the curve-fitting analysis, the amplitude reduction factor S2 0 was fixed to the best-fit value of 0.73, which was determined from fitting the reference sample of TiO_2 bulk. For the Ti-O/C_1 and Ti-C_2 shells, each of the Debye-Waller factors (σ^2), coordination numbers (N) and interatomic distances (R), energy shift (ΔE_0) were all treated as adjustable parameters. Herein, the number of adjustable parameters for the Ti_1/rGO sample is $N_{para} = 2 + 2 + 2 + 2 = 8 < N_{ipt} = 10$.

Computational models and methods. Ti_1/rGO and rGO computational models were constructed based on 6 × 6 × 1 supercells of graphene, and the box size was 14.76 Å × 14.76 Å × 16.70 Å. Neighboring slabs were separated through a vacuum of 15 Å to avoid interaction. The DFT calculations were performed with projector-augmented wave potentials and the Perdew–Burke–Ernzerhof (PBE) functional was implemented by the Vienna Ab-initio Simulation Package (VASP)[46,47]. Relaxations were performed through a conjugate-gradient algorithm. The selected energy convergence was 1×10^{-4} eV/atom and force convergence was 0.05 eV/Å. The cutoff energy was set to 400 eV. A Monkhorst-Pack point sampling of 4 × 4 × 1 was adopted. The occupancy of the one-electron states was revealed through Gaussian smearing (SIGMA = 0.05 eV).

***J*$_{sc}$-*V*$_{oc}$ measurement technique.** The starting point of the J_{sc}-V_{oc} technique is the single-diode approximation with negligible shunt resistance:

$$J(V, L, R_s) = J_0\left(1 - e^{\frac{q\,(V+R_sJ)}{nkT}}\right) + J_{sc}(L) \quad (1)$$

Here, L is the light intensity of the simulated sun light, J_0 the dark emission current, q the elementary charge, R_s the series resistance, n the ideality factor, k the Boltzmann constant and T the device temperature. $J_{sc}(L)$ and $V_{oc}(L)$ are measured for a series of light intensities L, which yields a pseudo-*J*-*V* curve $J^*_{sc}(V)$, where $J^*_{sc}(V) \equiv J_{sc}(L)$ with $V = V_{oc}(L)$. For $R_s = 0$, from (1) the following relationships are derived:

$$J(V_{oc}(L), L, R_s = 0) = 0 \;\rightarrow\; J_{sc}(L) = J_0\left(e^{\frac{q\,V_{OC}(L)}{nkT}} - 1\right)$$

$$J(V, 1\ sun, R_s = 0) = J_{sc}(1\ sun) - J^*_{sc}(V) \quad (2)$$

$J(V, 1\ sun, R_s = 0)$ is the *J*-*V* curve of the device with zero series resistance. In this work we call $J(V, 1\ sun, R_s = 0)$ the J_{sc}-V_{oc} curve. At J_{MPP} we have the following relationships for the *J*-*V* and the J_{sc}-V_{oc} curves, where for the latter V_0 is per definition the voltage at J_{MPP}:

$$J_{MPP} = J(V_{MPP}, 1\ sun, R_s) = J_0\left(1 - e^{\frac{q\,(V_{MPP}+R_sJ_{MPP})}{nkT}}\right) + J_{sc}(1\ sun)$$

$$J_{MPP} = J(V_0, 1\ sun, R_s = 0) = J_0\left(1 - e^{\frac{q\,V_0}{nkT}}\right) + J_{sc}(1\ sun)$$

$$\rightarrow V_{MPP} + R_sJ_{MPP} = V_0 \rightarrow R_s = (V_0 - V_{MPP})/J_{MPP}$$

To determine R_s at MPP we have to determine the voltage difference $\Delta V = V_o - V_{MPP}$ of the real *J*-*V* curve and the J_{sc}-V_{oc} curve at J_{MPP} and divide it by J_{MPP}.

Note that this technique is not restricted to devices which follow the singe-diode characteristics. In fact, the J_{sc}-V_{oc} method can be used for any solar cell that follows a characteristics of the form $J(V, L, R_s) = J_{dark}(V, R_s) + J_{sc}(L)$. One can also show that this method can even be applied if there is a non-negligible shunt resistance.

Reporting Summary. Further information on research design is available in the Nature Research Reporting Summary linked to this article.

Data availability

The data that support the findings of this study are available from the corresponding author upon reasonable request.

References

1. *Best Research Cell Efficiencies* (NREL, 2021); www.nrel.gov/pv/cell-efficiency.html
2. Khenkin, M. V., Katz, E. A., Abate, A., Bardizza, G., Berry, J. J., Brabec, C., Brunetti, F., Bulović, V., Burlingame, Q. and Di Carlo, A. Consensus statement for stability assessment and reporting for perovskite photovoltaics based on ISOS procedures. *Nat. Energy* **5**, 35-49 (2020).
3. Zheng, X., Hou, Y., Bao, C., Yin, J., Yuan, F., Huang, Z., Song, K., Liu, J., Troughton, J. and Gasparini, N. Managing grains and interfaces via ligand anchoring enables 22.3%-efficiency inverted perovskite solar cells. *Nat. Energy* **5**, 131-140 (2020).
4. Tress, W., Domanski, K., Carlsen, B., Agarwalla, A., Alharbi, E. A., Grätzel, M. and Hagfeldt, A. Performance of perovskite solar cells under simulated temperature-illumination real-world operating conditions. *Nat. Energy* **4**, 568-574 (2019).
5. Jiang, Y., Qiu, L., Juarez-Perez, E. J., Ono, L. K., Hu, Z., Liu, Z., Wu, Z., Meng, L., Wang, Q. and Qi, Y. Reduction of lead leakage from damaged lead halide perovskite solar modules using self-healing

polymer-based encapsulation. *Nat. Energy* **4**, 585-593 (2019).
6. Guerrero, A., You, J. B., Aranda, C., Kang, Y. S., Garcia-Belrnonte, G., Zhou, H. P., Bisquert, J. and Yang, Y. Interfacial degradation of planar lead halide perovskite solar cells. *ACS Nano* **10**, 218-224 (2016).
7. Rong, Y., Hu, Y., Mei, A., Tan, H., Saidaminov, M. I., Seok, S. I., McGehee, M. D., Sargent, E. H. and Han, H. Challenges for commercializing perovskite solar cells. *Science* **361**, eaat8235 (2018).
8. Wang, R., Mujahid, M., Duan, Y., Wang, Z. K., Xue, J. and Yang, Y. A review of perovskites solar cell stability. *Adv. Funct. Mater.* **29**, 1808843 (2019).
9. Domanski, K., Correa-Baena, J.-P., Mine, N., Nazeeruddin, M. K., Abate, A., Saliba, M., Tress, W., Hagfeldt, A. and Grätzel, M. Not all that glitters is gold: metal-migration-induced degradation in perovskite solar cells. *ACS Nano* **10**, 6306-6314 (2016).
10. Arora, N., Dar, M. I., Hinderhofer, A., Pellet, N., Schreiber, F., Zakeeruddin, S. M. and Grätzel, M. Perovskite solar cells with CuSCN hole extraction layers yield stabilized efficiencies greater than 20%. *Science* **358**, 768-771 (2017).
11. Rong, Y., Hou, X., Hu, Y., Mei, A., Liu, L., Wang, P. and Han, H. Synergy of ammonium chloride and moisture on perovskite crystallization for efficient printable mesoscopic solar cells. *Nat. Commun.* **8**, 1-8 (2017).
12. Mei, A., Li, X., Liu, L., Ku, Z., Liu, T., Rong, Y., Xu, M., Hu, M., Chen, J., Yang, Y. *et al.* A hole-conductor-free, fully printable mesoscopic perovskite solar cell with high stability. *Science* **345**, 295-298 (2014).
13. Zhang, H. Y., Xiao, J. Y., Shi, J. J., Su, H., Luo, Y. H., Li, D. M., Wu, H. J., Cheng, Y. B. and Meng, Q. B. Self-adhesive macroporous carbon electrodes for efficient and stable perovskite solar cells. *Adv. Funct. Mater.* **28**, 1802985 (2018).
14. Zhang, C., Wang, S., Zhang, H., Feng, Y., Tian, W., Yan, Y., Bian, J., Wang, Y., Jin, S. and Zakeeruddin, S. M. Efficient stable graphene-based perovskite solar cells with high flexibility in device assembling via modular architecture design. *Energy Environ. Sci.* **12**, 3585-3594 (2019).
15. Yan, K., Wei, Z., Li, J., Chen, H., Yi, Y., Zheng, X., Long, X., Wang, Z., Wang, J. and Xu, J. High-performance graphene-based hole conductor-free perovskite solar cells: Schottky junction enhanced hole extraction and electron blocking. *Small* **11**, 2269-2274 (2015).
16. Zhu, Y., Jia, S., Zheng, J., Lin, Y., Wu, Y. and Wang, J. Facile synthesis of nitrogen-doped graphene frameworks for enhanced performance of hole transport material-free perovskite solar cells. *J. Mater. Chem. C* **6**, 3097-3103 (2018).
17. Hadadian, M., Smått, J.-H. and Correa-Baena, J.-P. The role of carbon-based materials in enhancing the stability of perovskite solar cells. *Energy Environ. Sci.*, 1377-1407 (2020).
18. Arora, N., Dar, M. I., Akin, S., Uchida, R., Baumeler, T., Liu, Y., Zakeeruddin, S. M. and Grätzel, M. Low-cost and highly efficient carbon-based perovskite solar cells exhibiting excellent long-term operational and UV stability. *Small* **15**, 1904746 (2019).
19. Zheng, X., Chen, H., Li, Q., Yang, Y., Wei, Z., Bai, Y., Qiu, Y., Zhou, D., Wong, K. S. and Yang, S. Boron doping of multiwalled carbon nanotubes significantly enhances hole extraction in carbon-based perovskite solar cells. *Nano Lett.* **17**, 2496-2505 (2017).
20. Wu, Z., Liu, Z., Hu, Z., Hawash, Z., Qiu, L., Jiang, Y., Ono, L. K. and Qi, Y. Highly efficient and stable perovskite solar cells via modification of energy levels at the perovskite/carbon electrode interface. *Adv. Mater.*, 1804284 (2019).
21. You, P., Liu, Z., Tai, Q., Liu, S. and Yan, F. Efficient semitransparent perovskite solar cells with graphene electrodes. *Adv. Mater.* **27**, 3632-3638 (2015).
22. Zhou, J., Ren, Z., Li, S., Liang, Z., Surya, C. and Shen, H. Semi-transparent Cl-doped perovskite solar cells with graphene electrodes for tandem application. *Mater. Lett.* **220**, 82-85 (2018).
23. Lang, F., Gluba, M. A., Albrecht, S., Shargaieva, O., Rappich, J., Korte, L., Rech, B. and Nickel, N. H. In situ graphene doping as a route toward efficient perovskite tandem solar cells. *Phys. Status Solidi (a)* **213**, 1989-1996 (2016).
24. Chen, M., Zha, R., Yuan, Z., Jing, Q., Huang, Z., Yang, X., Yang, S., Zhao, X., Xu, D. and Zou, G. Boron and phosphorus co-doped carbon counter electrode for efficient hole-conductor-free perovskite solar cell. *Chem. Eng. J.* **313**, 791-800 (2017).
25. Chee, S. S., Seo, D., Kim, H., Jang, H., Lee, S., Moon, S. P., Lee, K. H., Kim, S. W., Choi, H. and Ham, M. H. Lowering the Schottky barrier height by graphene/Ag electrodes for high-mobility MoS_2 field-effect transistors. *Adv. Mater.* **31**, 1804422 (2019).
26. Kwon, K. C., Choi, K. S. and Kim, S. Y. Increased work function in few-layer graphene sheets via metal chloride doping. *Adv. Funct. Mater.* **22**, 4724-4731 (2012).
27. Zhou, S., Shang, L., Zhao, Y., Shi, R., Waterhouse, G. I., Huang, Y. C., Zheng, L. and Zhang, T. Pd single-atom catalysts on nitrogen-doped graphene for the highly selective photothermal hydrogenation of acetylene to ethylene. *Adv. Mater.* **31**, 1900509 (2019).

28. Peng, P., Shi, L., Huo, F., Mi, C., Wu, X., Zhang, S. and Xiang, Z. A pyrolysis-free path toward superiorly catalytic nitrogen-coordinated single atom. *Sci. Adv.* **5**, eaaw2322 (2019).
29. Chen, G., Liu, P., Liao, Z., Sun, F., He, Y., Zhong, H., Zhang, T., Zschech, E., Chen, M. and Wu, G. Zinc-mediated template synthesis of Fe-N-C electrocatalysts with densely accessible Fe-N_x active sites for efficient oxygen reduction. *Adv. Mater.*, 1907399 (2020).
30. Jiao, L. and Jiang, H.-L. Metal-organic-framework-based single-atom catalysts for energy applications. *Chem* (2019).
31. Xiang, H., Feng, W. and Chen, Y. Single-atom catalysts in catalytic biomedicine. *Adv. Mater.*, 1905994 (2020).
32. Samantaray, M. K., D'Elia, V., Pump, E., Falivene, L., Harb, M., Ould Chikh, S., Cavallo, L. and Basset, J.-M. The comparison between single atom catalysis and surface organometallic catalysis. *Chemical Reviews* (2019).
33. Huang, L., Chen, J., Gan, L., Wang, J. and Dong, S. Single-atom nanozymes. *Sci. Adv.* **5**, eaav5490 (2019).
34. Guan, J., Duan, Z., Zhang, F., Kelly, S. D., Si, R., Dupuis, M., Huang, Q., Chen, J. Q., Tang, C. and Li, C. Water oxidation on a mononuclear manganese heterogeneous catalyst. *Nat. Catal.* **1**, 870-877 (2018).
35. Zhang, B., Zhang, J., Shi, J., Tan, D., Liu, L., Zhang, F., Lu, C., Su, Z., Tan, X. and Cheng, X. Manganese acting as a high-performance heterogeneous electrocatalyst in carbon dioxide reduction. *Nat. Commun.* **10**, 1-8 (2019).
36. Gu, J., Hsu, C.-S., Bai, L., Chen, H. M. and Hu, X. Atomically dispersed Fe3+ sites catalyze efficient CO2 electroreduction to CO. *Science* **364**, 1091-1094 (2019).
37. Zhu, H., Liu, Y., Eickemeyer, F. T., Pan, L., Ren, D., Ruiz-Preciado, M. A., Carlsen, B., Yang, B., Dong, X. and Wang, Z. Tailored amphiphilic molecular mitigators for stable perovskite solar cells with 23.5% efficiency. *Adv. Mater.* **32**, 1907757 (2020).
38. Wolf, M. and Rauschenbach, H. Series resistance effects on solar cell measurements. *Adv. Energy Conv.* **3**, 455-479 (1963).
39. Mundhaas, N., Yu, Z. J., Bush, K. A., Wang, H. P., Häusele, J., Kavadiya, S., McGehee, M. D. and Holman, Z. C. Series resistance measurements of perovskite solar cells using J_{sc}-V_{oc} measurements. *Solar RRL* **3**, 1800378 (2019).
40. Zhang, C., Shi, Y., Wang, S., Dong, Q., Feng, Y., Wang, L., Wang, K., Shao, Y., Liu, Y. and Wang, S. Room-temperature solution-processed amorphous NbO x as an electron transport layer in high-efficiency photovoltaics. *J. Mater. Chem. A* **6**, 17882-17888 (2018).
41. Cai, X., Chen, K., Gao, X., Xu, C., Sun, M., Liu, G., Guo, X., Cai, Y., Huang, B. and Deng, J. Revealing atomic structure and oxidation states of dopants in charge-ordered nanoparticles for migration-promoted oxygen-exchange capacity. *Chem. Mater.* **31**, 5769-5777 (2019).
42. Cueva, P., Hovden, R., Mundy, J. A., Xin, H. L. and Muller, D. A. Data processing for atomic resolution electron energy loss spectroscopy. *Microsc. Microanal.* **18**, 667-675 (2012).
43. Newville, M. IFEFFIT: interactive XAFS analysis and FEFF fitting. *J. Synchrotron Radiat.* **8**, 322-324 (2001).
44. Ravel, B. and Newville, M. ATHENA, ARTEMIS, HEPHAESTUS: data analysis for X-ray absorption spectroscopy using IFEFFIT. *J. Synchrotron Radiat.* **12**, 537-541 (2005).
45. Ankudinov, A. L., Ravel, B., Rehr, J. and Conradson, S. Real-space multiple-scattering calculation and interpretation of x-ray-absorption near-edge structure. *Phys. Rev. B* **58**, 7565 (1998).
46. Kresse, G. and Furthmüller, J. Efficiency of ab-initio total energy calculations for metals and semiconductors using a plane-wave basis set. *Comput. Mater. Sci.* **6**, 15-50 (1996).
47. Kresse, G. and Furthmüller, J. Efficient iterative schemes for ab initio total-energy calculations using a plane-wave basis set. *Phys. Rev. B* **54**, 11169 (1996).

Acknowledgments

This work was financially supported by the National Natural Science Foundation of China (51872036, 51773025, 11504046), LiaoNing Revitalization Talents Program (XLYC2007038, XLYC2008032), Dalian science and technology innovation fund (2018J12GX033, 2019J12GX032), and special funds for science and technology development under the guidance of the central government (2021JH6/10500152). Prof. N. W. thanks the financial support from the Hong Kong Research Grants Council (Project Nos. 16306818 and N_HKUST624/19). C. Y. Z. would like to thank the Chinese Scholarship Council for their financial support to his in-split Ph.D. study in Switzerland. M.G. thanks the financial support from the European Union's

Horizon 2020 research and innovation programme under grant agreement No 881603.

Author contributions

Y. T. S. and C. Y. Z. proposed the idea, designed the project and organized the manuscript, C. Y. Z. carried out the experiments including material characterizations, device fabrication and measurements. M. G. supervised the experimental investigation and manuscript modification. C. Z. contributed to material design, STEM characterization, structure analysis and manuscript preparation. W. L. conducted XANES and EXAFS measurements and analyzed the chemical structure of Ti_1/rGO. S. X. L. prepared Ti_1/rGO and conducted DFT calculations. F. T. E. conducted and interpreted the J_{sc}-V_{oc} measurements. X. B. C. and N. W. conducted and interpreted the EELS characterization. S. M. Z. helped on manuscript organization and project coordination. K. Z. conducted the HTEM, EDX mapping characterizations and XAFS measurements. J. M. B. contributed to the analysis of the characterizations around interface. H. W. Z. helped on the device fabrication. Z. W. W. modified the manuscript. J. W. Z analyzed the chemical structure of Ti_1/rGO. Y. D. W. contributed to mechanical pressure measurement. J. W. H., C. C. X. and H. R. M. offered help on material preparations and XPS/UPS characterizations. All authors contributed to results discussion and manuscript writing.

Competing interests

The authors declare no competing interests.

Additional information

Supplementary information is available for this paper at https://doi.org/

Correspondence and requests for materials should be addressed to C. Z., M. G. or Y. T. S.

Reprints and permissions information is available at www.nature.com/reprints.

Publisher's note Springer Nature remains neutral with regard to jurisdictional claims in published maps and institutional affiliations.